Ocean Dynamics
https://doi.org/10.1007/s10236-023-01565-9

Seasonal variability of eddy characteristics and energetics in the Kuroshio Extension

Chen Yang[1,2] · Haiyuan Yang[1,2] · Zhaohui Chen[1,2] · Bolan Gan[1,2] · Yongzheng Liu[1,2] · Lixin Wu[1,2]

Received: 4 July 2022 / Accepted: 29 June 2023

Abstract
Based on the eddy-resolving Four-dimensional variational Ocean Re-Analysis for the Western North Pacific over 30 years (FORA-WNP30) product, this study investigates the seasonal evolution of mesoscale eddy characteristics and underlying mechanisms in the Kuroshio Extension (KE) region. In the upstream region, eddies are stretched in the zonal direction and characterized by higher activity in summer and autumn. Energy analysis illustrates that baroclinic instability associated with the horizontal buoyancy flux is responsible for the seasonal variability. In the downstream region, in comparison, eddies tend to be stretched in the meridional direction. Eddy kinetic energy (EKE) level in this region is mainly regulated by the upstream through pressure work. During 1993–2013, the EKE level does not change in the upstream region but it depicts an increasing trend in the downstream region. This evolution reflects the decadal variability of the KE system associated with the Pacific Decadal Oscillation.

Keywords Kuroshio Extension · Eddy kinetic energy · Eddy energy spectral · Eddy energy · EKE trend

1 Introduction

The Kuroshio Current, one of the strongest western boundary currents in the global ocean, transports large amounts of water and heat from the tropical region northward to the North Pacific. It separates from the east coast of Japan near 35° N and is renamed as the Kuroshio Extension (KE). As an inertial jet, the KE is characterized by strong recirculation gyre, time-varying path, and large meanders (Mizuno and White 1983; Wijffels et al. 1998; Qiu and Chen 2005). Overlaid by intense westerly and active atmospheric storms, the KE has been proved to be a key region of ocean circulation and air-sea interaction in mid-latitudes (Qiu and Kelly 1993; Cornillon and Park 2001; Vivier et al. 2002; Nonaka and Xie 2003; Xu et al. 2010; Ma et al. 2016).

In addition to its large-scale characteristics, the KE is also abundant with energetic mesoscale eddies (Jayne et al. 2009; Scharffenberg and Stammer 2010; Waterman et al. 2011; Nakamura et al. 2015; Yang et al. 2017; Dong et al. 2017). Satellite observations reveal that anticyclonic eddies (AEs) are mainly observed along the northern flank of the KE, while cyclonic eddies (CEs) are more frequently distributed along the southern flank (Itoh and Yasuda 2010; Sasaki and Minobe 2015). After generation, both AEs and CEs propagate westward with a speed close to baroclinic Rossby waves and last for 8–13 weeks on average (Sasaki and Minobe 2015; Meng et al. 2021). Further explorations indicate that eddies in this region are generated through shear instability and meander development of the KE jet (Waterman et al. 2011; Ji et al. 2018; Matsuta and Masumoto 2021) or originate from the central North Pacific Ocean (Deser et al. 1999; Qiu 2003).

With the accumulation of observations over the past 30 years, many studies have focused on the decadal variability of eddy activity, which is associated with the fluctuations of dynamical state of KE (Qiu and Chen 2005, Qiu et al. 2014; Kelly et al. 2010; Sasaki et al. 2013; Jiang et al. 2017; Yang et al. 2018; Wang and Tang 2022). During the stable state, the KE jet has a straighter path and larger transport, and eddy kinetic energy (EKE) in the upstream (downstream) is smaller (larger). The reverse is true for the unstable period. To date, several potential factors associated

Responsible Editor: Helen Phillips

✉ Haiyuan Yang
yanghaiyuan@ouc.edu.cn

[1] Frontier Science Center for Deep Ocean Multispheres and Earth System (FDOMES) and Physical Oceanography Laboratory, Ocean University of China, 238 Songling Road, Qingdao 266100, China

[2] Laoshan Laboratory, Qingdao, China

Published online: 11 July 2023

with this decadal variability, such as the instability of background flow (Wang et al. 2017; Yang et al. 2017, 2018), wind-induced Rossby wave adjustment (Miller et al. 1998; Deser et al. 1999; Seager et al. 2001; Kwon and Deser 2007; Ceballos et al. 2009; Sasaki and Schneider 2011), and the effect of topography (Qiu and Chen 2005) have been extensively discussed.

Besides the decadal variability, the seasonality of EKE in the vicinity of KE has also attracted much attention (Tai and White 1990; Stammer and Wunsch 1999; Ducet and Le Traon 2001; Scharffenberg and Stammer 2010; Zhai 2017; Yang and San Liang 2018; Wang and Pierini 2020). Based on satellite observations, Ji et al. (2018) pointed out that the number of eddies tends to be larger (smaller) and EKE tends to be higher (lower) in summer (winter). Meng et al. (2021) suggested that more eddies are found in June, with larger amplitude and larger radius, than in December. Yang and San Liang (2018) found that the anomaly of EKE relative to the annual mean value is different in summer and winter. In summer (winter), large positive (negative) anomaly of EKE is mainly found in 142° E–155° E, 31° N–39° N. Mechanisms underlying the seasonal-varying eddy field have also been proposed in previous studies. Regulated by the surface buoyancy field (Cronin et al. 2013) and Kuroshio transport south of Japan (Imawaki et al. 2001), the KE jet and available potential energy (APE) stored in the mean stratification depict obvious seasonal variability, which influences eddy generation in the upstream KE (Yang and San Liang 2018; Wang and Pierini 2020). Compared with the upstream, the intensity of EKE in the downstream region is much weaker and two potential energy sources have been suggested. By analyzing local eddy energy generation, Yang and San Liang (2018) emphasized the role of baroclinic instability (BC) in regulating the seasonal variations in eddy fields. Others, however, argue that eddies give energy back to mean flow in this region and imply the importance of advection effect (Berloff and McWilliams 1999; Waterman and Hoskins 2013; Yang et al. 2018).

These previous studies have significantly improved our knowledge on the seasonality of the eddy activity in the KE region; however, some important issues remain unsolved. Firstly, eddy characteristics, such as the EKE power spectral density and eddy shapes, are useful indicators for eddy-mean flow interactions (Qiu et al. 2008; Marshall et al. 2012; Waterman and Hoskins 2013) and are not studied at seasonal timescales. Secondly, the dominant energy source of eddy generation in regulating the EKE seasonal variability, especially in the downstream KE, is still controversial (Yang and San Liang 2018; Yang et al. 2018). Thirdly, previous studies have proved that oceanic response to global warming varies seasonally (Yang and Wu 2012; Huang 2015; Wang et al. 2021). Given that the western boundary currents have experienced the accelerated warming since the 1900s, especially in the past 30 years (Wu et al. 2012; Hu et al. 2020), it is important to confirm whether the seasonality of EKE has changed.

In this study, the abovementioned issues regarding the seasonal variability of EKE in the KE region are examined, on the basis of an eddy-resolving reanalysis product. Based on previous estimations, the upstream and downstream KE depict different features in dynamical state of flow and EKE level evolution (Qiu and Chen 2005; Jiang et al. 2017), eddy generation mechanism (Yang and San Liang 2018; Yang et al. 2018), and eddy-mean flow interaction (Waterman and Hoskins 2013; Yang et al. 2018). Actually, as will be shown later, the seasonal evolution of eddy characteristics and energetics is different in the upstream and downstream KE. Therefore, upstream and downstream region of the KE is also investigated in the following discussions. The rest of the paper is organized as follows: Section 2 gives a brief description of the data used in this study. In Section 3, a detailed study of the eddy characteristics and energetics is presented, followed by their changes during 1993–2013. The paper ends with a summary and further discussion in Section 4.

2 Data

2.1 FORA-WNP30 data

In this study, seasonal variability of eddy activity in the KE region is analyzed using the Four-dimensional variational Ocean Re-Analysis for the Western North Pacific over 30 years (FORA-WNP30) product (http://synthesis.jamstec.go.jp/FORA/e/; Usui et al. 2017). It is based on the western North Pacific version of the Meteorological Research Institute (MRI) Community Ocean Model version 2.4 (MRI.COM-WNP; Tsujino et al. 2006). MRI.COM-WNP solves the primitive equations under the hydrostatic and the Boussinesq approximations in the western North Pacific (117° E–160° W, 15° N–65° N). The horizontal resolution of this model is not constant: it is 1/10° within 117° E–160° E and 1/6° in 160° E–160° W zonally, while 1/10° within 15° N–50° N and 1/6° in 50° N–65° N in the meridional direction. In the vertical direction, there are 54 levels with thickness varying from 1 m at the surface to 600 m near the bottom at a maximum depth of 6300 m. A biharmonic operator is used in the horizontal mixing and friction, while the vertical viscosity and diffusivity are determined in accordance with Noh and Jin Kim (1999). MRI.COM-WNP is driven by the atmospheric forcing derived from the Japanese 55-year Reanalysis (JRA-55; Kobayashi et al. 2015). With the application of the multivariate four-dimensional variational (4DVAR) analysis scheme, namely, the MRI Multivariate Ocean Variational Estimation system

(MOVE-4DVAR), the model assimilates several available in situ and satellite observations (e.g., in situ temperature and salinity profiles, sea surface temperature, sea surface height (SSH), and sea ice concentration), which makes this product reliable for process analysis. Because of its good performance, FORA-WNP30 has been used to explore multiscale oceanic dynamics in the North Pacific region (Jing et al. 2019; Wang and Pierini 2020; Long et al. 2021). In this paper, daily mean data in the region (140° E–180° E, 25° N–45° N) during 1993–2013 is used.

2.2 Satellite observation

To validate the FORA-simulated eddy activity, the merged absolute dynamic topography (ADT) product (https://www.aviso.altimetry.fr/) is used in our analysis. Using data from the Jason-3, Sentinel-3A, HY-2A, Saral/AltiKa, Cryosat-2, Jason-2, Jason-1, T/P, ENVISAT, GFO, and ERS1/2 altimeter missions, the data is processed by the DUACS multimission altimeter data processing system and distributed by Archiving, Validation, and Interpretation of Satellite Oceanographic data (AVISO). The temporal resolution of the dataset is 1 day and the horizontal resolution of the dataset is 0.25°, which is useful to analyze mesoscale eddies. As for the FORA-WNP30 dataset, the SSH data from 1993 to 2013 in the region (140° E–180° E, 25° N–45° N) is used.

2.3 Reanalysis data

To validate the results of wind evolution during 1993–2013, JRA-55 and the European Centre for Medium-Range Weather Forecasts ERA5 reanalysis products (ECMWF ERA5; https://rda.ucar.edu/datasets/ds633.1/; Hersbach et al. 2020) are used.

The first full-observing-system reanalysis product JRA-55 covers the period from 1958, when the global radiosonde observing system was established (Kobayashi et al. 2015). JRA-55 has been transformed from the TL319L60 grid to a regular latitude–longitude Gaussian grid, 320 latitudes by 640 longitudes, nominally 0.5625° in the meridional and zonal directions. According to Harada et al. (2016) and Miao et al. (2020), JRA-55 offers good estimates of wind speed over the Northern Hemisphere. As the most recent (5th generation) global atmospheric reanalysis of the European Centre for Medium-Range Weather Forecasts (ECMWF), ERA5 stands out for its high resolution as well as for a large amount of assimilated observations (Hersbach et al. 2020). ERA5 provides global, hourly estimates of atmospheric variables, at a horizontal resolution of 31 km (0.25°) and 137 vertical levels from the surface to 0.01 hPa. Previous studies pointed out that ERA5 works well for the representation of surface and low-level winds over the ocean (Olauson 2018; Belmonte Rivas and Stoffelen 2019; Kalverla et al. 2019). The assimilation of infrared radiances and winds from GMS/MTSAT/Himawari geostationary satellites along 140° E makes it a reliable choice for the research on large-scale air temperature and wind fields in the KE region. In this study, we will focus on the region (130° E–120° W, 15° N–65° N) during the period from 1993 to 2013.

3 Results

3.1 Seasonal variability of EKE

Before analyzing the seasonal cycle of EKE in the KE region, it is necessary to quantify whether FORA can capture the seasonal cycle of mesoscale eddies as observed by satellite. Here, EKE is defined as

$$\mathrm{EKE} = \frac{1}{2}(u'^2 + v'^2), \tag{1}$$

where u' and v' denote zonal and meridional surface velocity deviation from their 240-day-running-mean values, consistent with previous studies (Itoh and Yasuda 2010; Yang et al. 2017). Changing the cutoff period from 180 to 300 days does not generate a significant difference in the following analysis. It is noted that the resolution of FORA is higher than that of satellite observations. To make a comparison between these two datasets, a two-dimensional interpolation is applied to FORA data. Figure 1a and b reveals that the spatial patterns of SSH and EKE simulated by FORA resemble those of AVISO. Two meanders appear at approximately 145° E and 150° E with a meridional span of 4° from 33° N to 37° N, consistent with Lan et al. (2003). Strong eddy activity is concentrated within the area of 145° E–150° E and 32° N–36° N, with the maximum located around the first trough of KE (146° E–148° E, 34° N–36° N). In addition to the spatial pattern, seasonal variability of EKE in the upstream (142° E–152° E, 31° N–39° N), downstream (152° E–170° E, 31° N–39° N), and entire KE (142° E–170° E, 31° N–39° N) is also successfully simulated by FORA (Stammer and Wunsch 1999; Scharffenberg and Stammer 2010; Yang and San Liang 2018; Fig. 1c and d). In both upstream and downstream regions, high EKE level is found in summer (June–August; JJA) and autumn (September–November; SON), while low eddy activity appears in spring (March–May; MAM) and winter (December-February; DJF). The amplitude of seasonal variability of EKE is about 0.023 (0.015) m s in the upstream (downstream) region, close to observation as well. Overall, FORA reasonably reproduces the seasonal variability of eddy activity in the upstream and downstream KE. Next, we will use it to investigate the eddy dynamics.

To understand the characteristics of mesoscale eddies, we calculate power spectral density

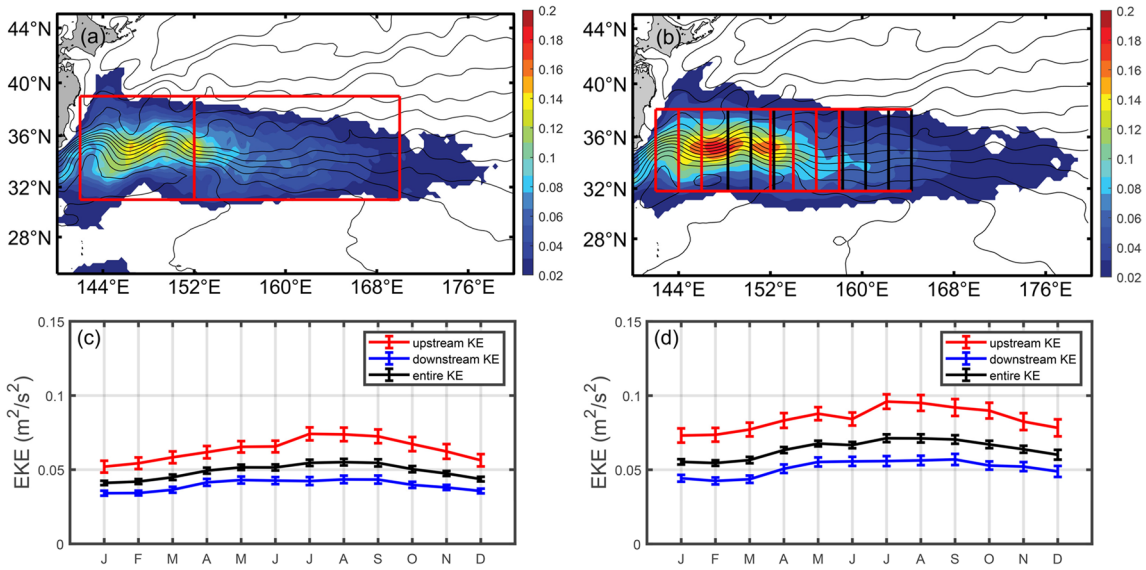

Fig. 1 **a** Mean EKE during 1993–2013 based on satellite observation (colored shading; m^2/s^2). Black contours indicate SSH isolines. Red boxes indicate the upstream and downstream regions, respectively. **b** Mean EKE during 1993–2013 based on FORA (colored shading; m^2/s^2). Black contours indicate SSH isolines. Seven overlapping boxes with 64×64 grid points (6.4°×6.4°) are shown. The red meridional lines indicate the west boundaries of the boxes, while the black meridional lines represent the east boundaries of the boxes. Seasonal cycle of EKE averaged in upstream KE, downstream KE, and entire KE region from **c** satellite observation and **d** FORA. Error bars indicate the standard errors

$$E(k_x, k_y, t) = \frac{1}{2}\left(u' u'^{*} + \hat{v}' \hat{v}'^{*}\right), \tag{2}$$

as a function of zonal and meridional wavenumbers, k_x and k_y. Caret and star denote discrete Fourier transform and corresponding complex conjugate, respectively. Following Qiu et al. (2008), the velocity anomaly data is preprocessed as follows. The velocity anomaly is partitioned into seven overlapping boxes (the boxes in Fig. 1b) with 64×64 grid points (6.4°×6.4°). The average of three boxes is used to evaluate the EKE spectra in the upstream KE, whereas four boxes are used for the downstream KE. The latitude and longitude ranges of seven boxes are shown in Table 1. By fitting a bilinear plane via least squares, the velocity anomaly fields are detrended for each box and each time step. A Hanning window is then applied to the detrended data.

The EKE power spectral density distributions in the upstream and downstream KE regions are shown in Figs. 2 and 3, respectively. In the upstream region, the power spectral density reaches the maximum (minimum) in summer (winter). A higher energy level is found at larger k_y than k_x ranges all year round, suggesting that eddies in this region are more zonally elongated. Compared to the upstream region, the power spectral density in the downstream region reaches the maximum in autumn. A high energy level is found to appear at larger k_x range in the downstream region (Fig. 3), which indicates that eddies tend to be meridionally elongated. The difference of eddy shape between the upstream and the downstream regions is further confirmed by estimating the eddy elongation parameter (Fig. 4)

$$M = \frac{1}{2}\left(u'^2 - v'^2\right). \tag{3}$$

As an element of eddy Reynolds stresses, M is suggested to be a useful indicator to present the interaction between eddies and mean flow (Waterman and Hoskins 2013). When M is negative (positive), eddies are meridionally (zonally) elongated and more energy is confined to large k_x (k_y) than k_y (k_x). In the upstream region, M depicts large positive values around the first crest of the meandering KE. In contrast, M is characterized by negative values in the downstream east of 152° E. The distribution of M illustrates that eddies tend to be elongated along (across) the mean jet axis in the upstream region (downstream), consistent with the spectral analysis. According to Waterman and Hoskins (2013), this phenomenon implies that eddies draw energy from mean flow in the upstream region and give energy back to mean flow in the downstream region.

Table 1 The latitude and longitude ranges of 7 boxes (3 boxes in the upstream region and 4 boxes in the downstream region)

Box number	Region	Latitude range	Longitude range
1	Upstream		142° E–148.3° E
2	Upstream		144° E–150.3° E
3	Upstream		146° E–152.3° E
4	Downstream	31.8° N–38.1° N	152° E–158.3° E
5	Downstream		154° E–160.3° E
6	Downstream		156° E–162.3° E
7	Downstream		158° E–164.3° E

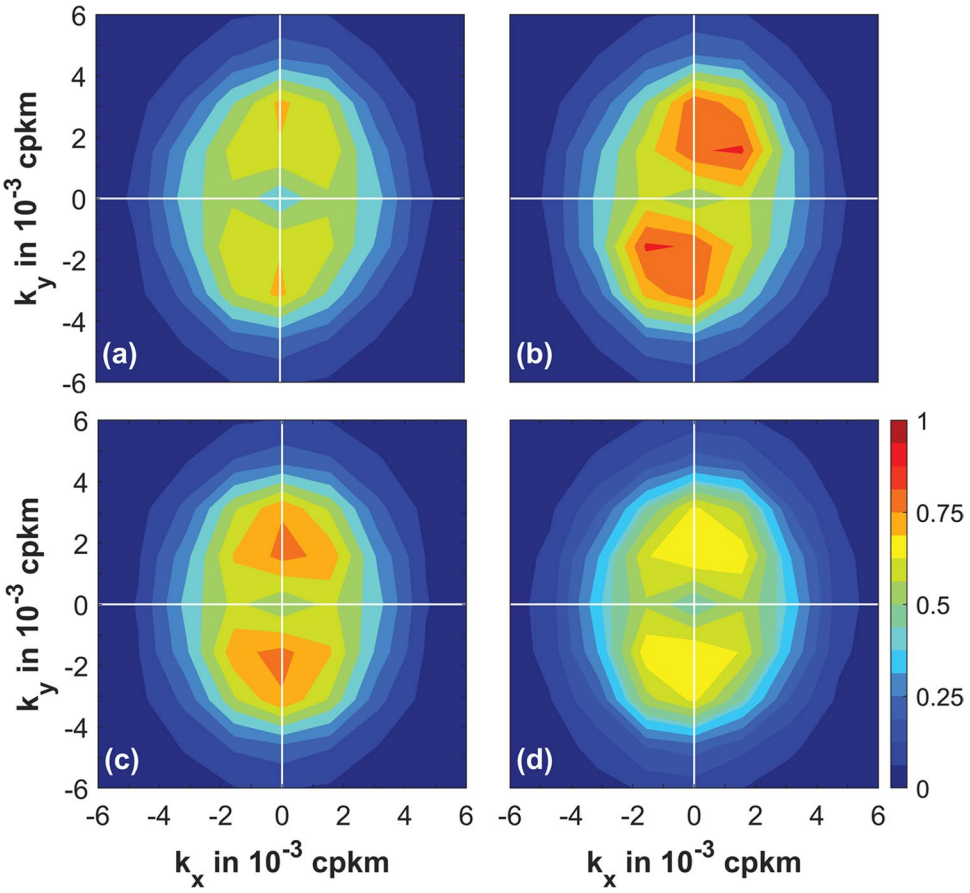

Fig. 2 Normalized EKE power spectral density distributions as a function of k_x and k_y in the upstream KE region in **a** spring, **b** summer, **c** autumn, and **d** Winter

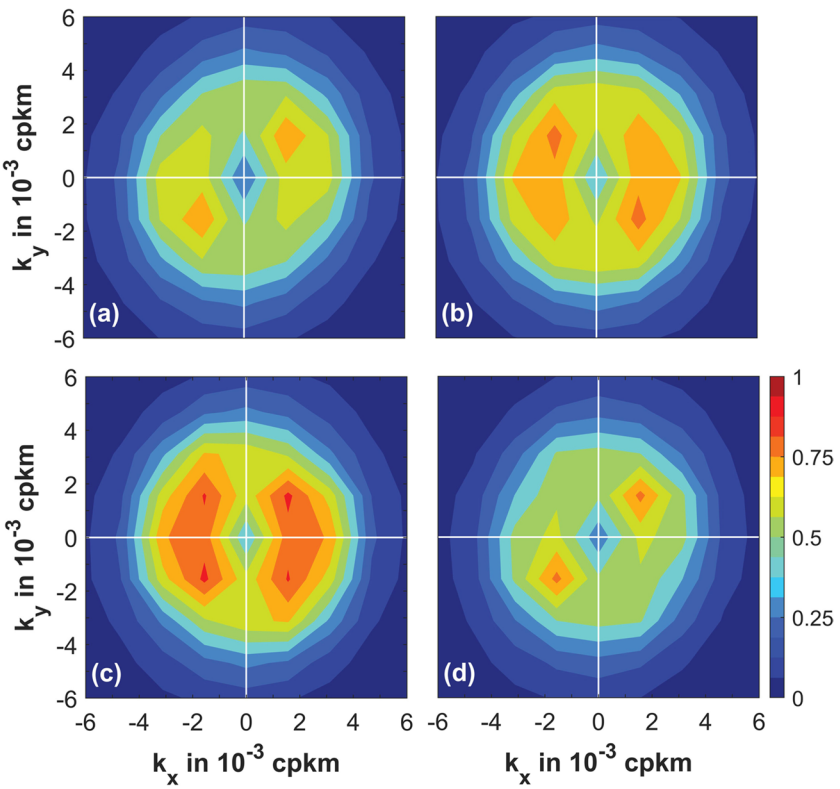

Fig. 3 Normalized EKE power spectral density distributions as a function of k_x and k_y in the downstream KE region in **a** spring, **b** summer, **c** autumn, and **d** winter

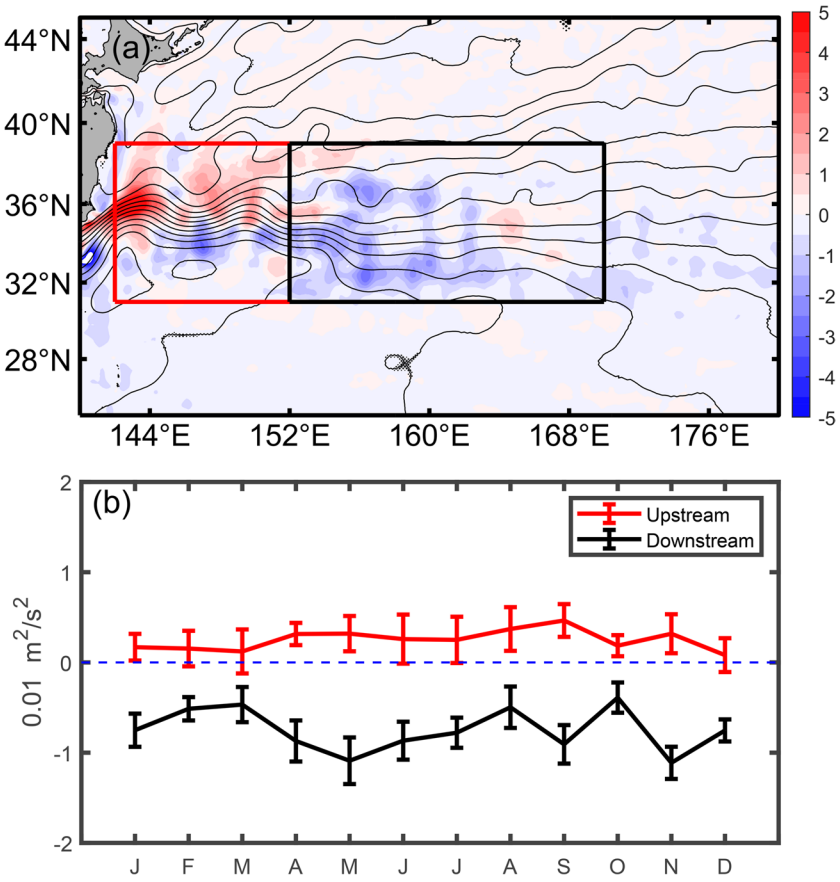

Fig. 4 **a** Spatial distribution of M (colored shading; 0.01 m^2/s^2) based on FORA. Contours are state-mean SSH isolines. Red and black boxes indicate the upstream and downstream regions, respectively. **b** Annual cycle of M averaged in the upstream region (142° E–152° E, 31° N–39° N) and the downstream region (152° E–170°E, 31°N–39° N). Error bars indicate the standard errors

In the following section, we will further confirm this based on eddy energy budget analysis.

3.2 Energetics

To clarify the dominant energy sources responsible for the seasonal variability of eddy activity, we estimate the energy obtained by eddies through BC and barotropic instability (BT; von Storch et al. 2012 and Chen et al. 2014):

$$\mathrm{BC} = -\frac{g^2}{\rho_0 N^2}\rho' {v_h}' \cdot \nabla_h \bar{\rho}, \tag{4a}$$

$$\mathrm{BT} = -\rho_0(u' {v_h}' \cdot \nabla_h \bar{u} + v' {v_h}' \cdot \nabla_h \bar{v}), \tag{4b}$$

where g is gravitational acceleration, N^2 is the square of the buoyancy frequency, and ρ_0 is the background density 1025 kg/m^3. The symbol $\mathbf{v}_h$ means horizontal velocity vector, and ∇_h represents the horizontal gradient operator. Physically, BC (unit: W/m^3) denotes the energy between mean flow and eddy through vertical shear, and BT (unit: W/m^3) represents the energy exchange between mean flow and eddy through horizontal shear. Based on previous studies, they are the main local energy sources of mesoscale eddies in the global ocean (Gill et al. 1974; Stammer 1998; Noh et al. 2007; von Storch et al. 2012; Chen et al. 2014; Wang et al. 2017). In addition to local energy exchange, eddy activity can also be regulated by remote regions through non-local effects (Chen et al. 2014; Yang et al. 2018). Physically, this non-local energy exchange (Q; unit: W/m.^{3}) involves the energy flux divergence through eddy-induced advection (Adv) and the work done by eddies on the surrounding environment through eddy-induced pressure (Pre). The equation is as follows:

$$Q = -\nabla \cdot [\underbrace{\frac{1}{2}\rho_0 \mathbf{v}_h\left(u'^2 + v'^2\right)}_{Adv} + \underbrace{p' {\mathbf{v}_h}'}_{Pre}] \tag{5}$$

The symbol p indicates the pressure of the water column above a specific depth.

The seasonal cycle of the volume integral values of EKE, BC, BT, and Q is shown in Fig. 5. To get a better knowledge of energy exchange, their horizontal distributions at the sea surface are presented in Fig. 6. Consistent with the distribution of EKE spectral energy (Fig. 2) and M (Fig. 4), significant BC is detected along the KE jet with the maximum occupying the first crest of meander at 145° E. In the upstream region, negative patches are found near the trough around 146° E–148° E, which may be caused by the vertical velocity

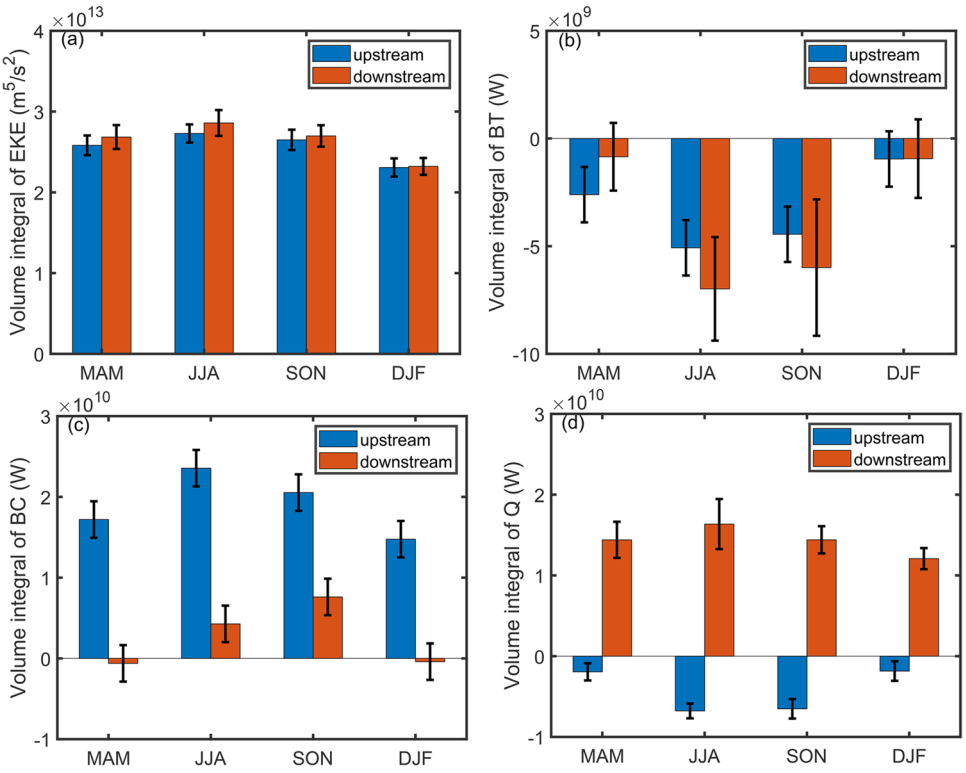

Fig. 5 Seasonal cycle of the volume integral of **a** EKE, **b** BT, **c** BC, and **d** Q. The volume integral is conducted in the upper 600 m over the upstream KE (142° E–152° E, 31° N–39° N) and downstream KE (152° E–170° E, 31° N–39° N). Error bars indicate the standard errors

anomaly related to cold-core rings in that area (Bishop 2013). According to Fig. 5b and d, BT and Q act as EKE sinks in the upstream region throughout the year. Quantitatively, BC exhibits a much larger magnitude than the other two terms, and the correlation coefficient between BC and EKE reaches 0.92 (Fig. 5a and c), suggesting its predominant role in regulating the seasonal variability of mesoscale eddy activity. To further explore the dynamics underlying seasonal evolution of BC, we respectively estimate background buoyancy frequency (N^2) and eddy-induced buoyancy flux in Eq. (6). In

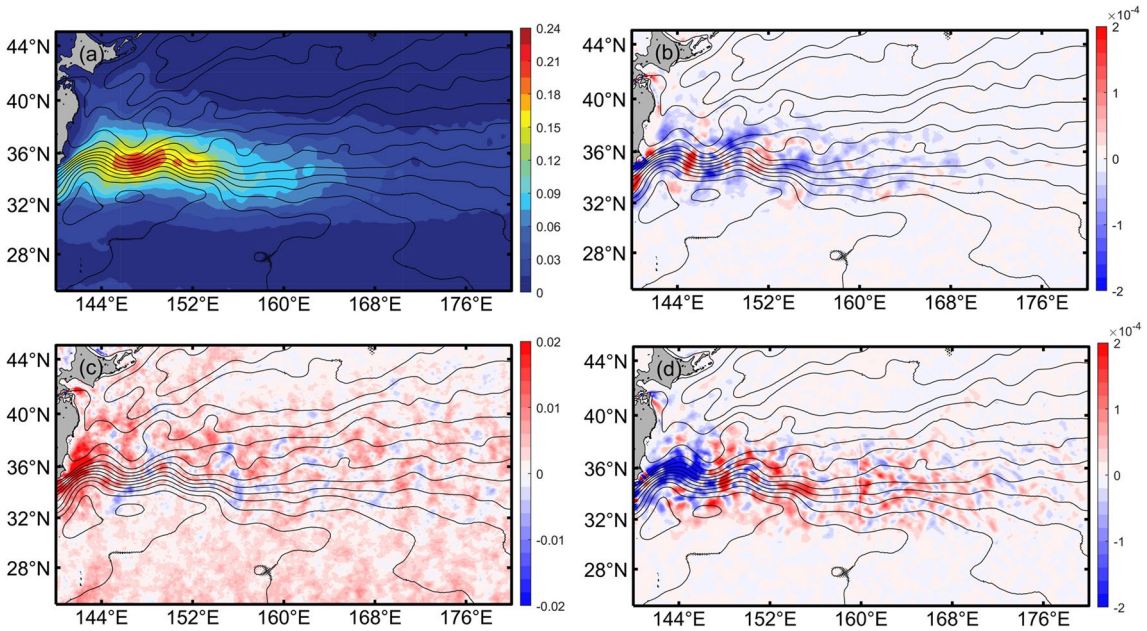

Fig. 6 Spatial distribution of **a** EKE (unit: m^2/s^2), **b** BT (unit: W/m^3), **c** BC (unit: W/m^3), and **d** Q (unit: W/m^3) at the sea surface based on FORA. Contours are state-mean SSH isolines

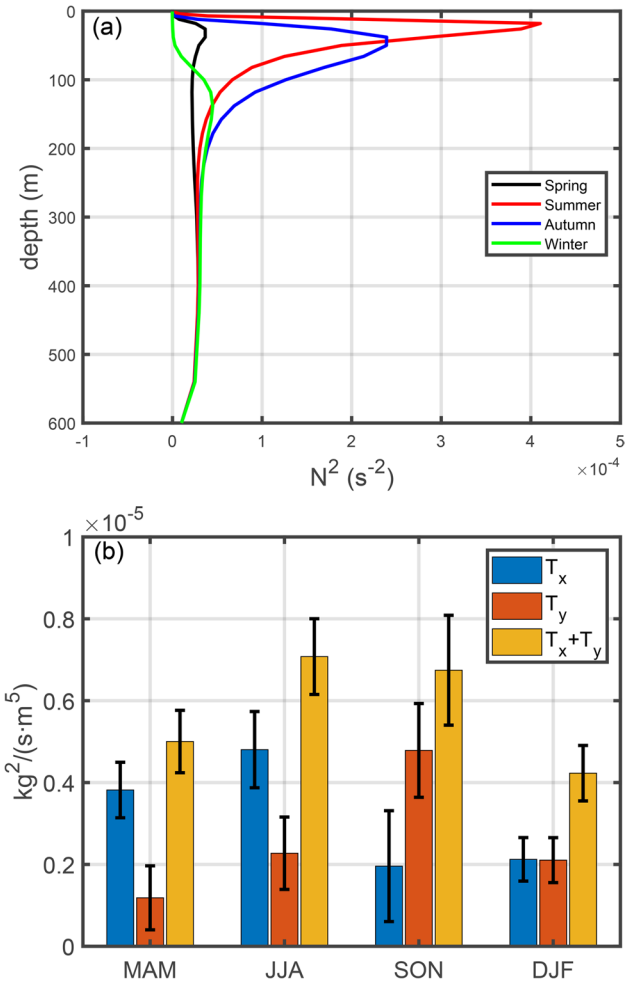

Fig. 7 **a** Distribution of N^2 in four seasons averaged within the upstream KE region (142° E–152° E, 31° N–39° N) in the upper 600 m. **b** Seasonal cycle of depth-integrated (upper 600-m depth) T_x, T_y, and (T_x+T_y) averaged over the upstream KE region. Error bars indicate the standard errors

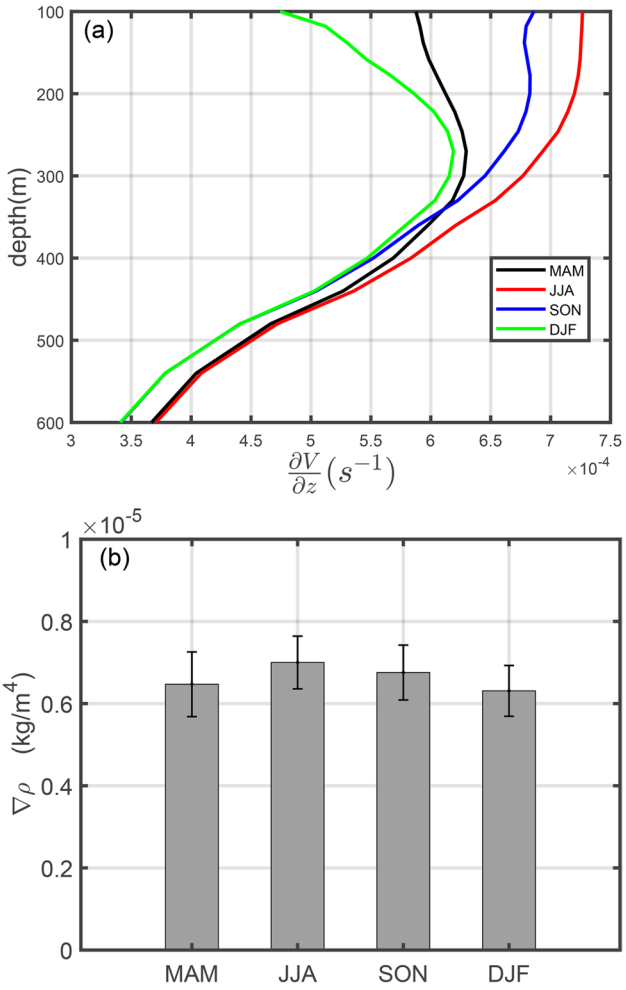

Fig. 8 **a** Distribution of vertical shear of horizontal speed ($\frac{\partial V}{\partial z}=\frac{\partial\sqrt{(u^2+v^2)}}{\partial z}$) in four seasons averaged over the upstream KE region (142° E–152° E, 31° N–39° N). **b** Seasonal cycle of horizontal density gradient ($\nabla\rho=\sqrt{\left(\frac{\partial\rho}{\partial x}\right)^2+\left(\frac{\partial\rho}{\partial y}\right)^2}$) averaged over the upstream KE region at the 250 m. Error bars indicate the standard errors

particular, the eddy-induced buoyancy flux is divided into two parts (Wang and Pierini 2020):

$$T_x=-\rho' u'\frac{\partial\overline{\rho}}{\partial x}, \tag{6a}$$

$$T_y=-\rho' v'\frac{\partial\overline{\rho}}{\partial y}. \tag{6b}$$

Here, T_x and T_y represent eddy buoyancy flux down the gradient of density in the zonal and meridional directions, respectively. Figure 7a shows the N^2 in four seasons, in which it reaches the maximum in summer and minimum in winter. The evolution favors a smaller BC in summer and a larger BC in winter, which is inconsistent with the BC change. Figure 7b illustrates the seasonal evolution of depth-integrated (upper 600-m depth) T_x, T_y, and (T_x+T_y) averaged over the upstream KE region. Similar to BC, (T_x+T_y) is stronger in summer and weaker in winter. By estimating the correlation coefficient of monthly mean (T_x+T_y) and BC over the period 1993–2013, it is found that the coefficient reaches 0.85 (significant at the 90% level based on the Student *t*-test), suggesting that eddy buoyancy flux is responsible for the evolution of BC. Both T_x and T_y contribute to the seasonal variability of (T_x+T_y). In spring and summer, T_x is the main component of (T_x+T_y), accounting for 76.3% and 67.9% of (T_x+T_y). In comparison, T_y makes up 71.0% of (T_x+T_y) in autumn. In winter, T_x and T_y are almost equal (50.2% and 49.8%).

In addition to the interpretation in terms of energy, the seasonal evolution of baroclinicity of the KE jet can also be

understood through its physical state. Figure 8a shows the vertical shear of velocity ($\frac{\partial V}{\partial z} = \frac{\partial\sqrt{(u^2+v^2)}}{\partial z}$) in the upstream region. In accordance with BC, the vertical shear of velocity is much stronger in summer and autumn, especially in the upper 300 m. Based on thermal wind balance, the vertical shear is proportional to the horizontal gradient of density ($\frac{\partial u}{\partial z} = -\frac{g}{f\rho}\frac{\partial \rho}{\partial y}, \frac{\partial v}{\partial z} = \frac{g}{f\rho}\frac{\partial \rho}{\partial x}$). At the depth of 250 m, the density front undergoes a weak annual cycle with a suggestion of stronger gradients in summer, weaker in winter (Fig. 8b). This phenomenon could be attributed to the seasonal evolution of surface buoyancy forcing. In winter, large air-sea temperature difference and strong surface wind induce a significant heat loss and intense mixing in the upper ocean (Kelly et al. 2010), which deepens the mixed layer and favors a downward momentum flux. Correspondingly, a smaller vertical shear of the velocity is detected. By contrast, the weaker surface buoyancy forcing in summer results in a shallower mixed layer and larger vertical shear of the velocity.

As shown in the above discussion, BC plays a dominant role in forming the EKE seasonality in the upstream KE region. From Fig. 5, we know that BC is the main source of EKE in the upstream region, while for the downstream region, the energy source is mainly Q. Q is comprised of the energy flux divergence through eddy-induced advection and the work done through eddy-induced pressure, and the role of advection and pressure work at the boundaries of the downstream KE is shown in Table 2. We do not present the numbers for upstream, because Q is not an important factor in the upstream (Fig. 5). Compared to advection, pressure work is about 10 times larger and its seasonal evolution is almost the same as the downstream EKE. As such, we conclude that Q is dominated by eddy-induced pressure work, especially from the west boundary, consistent with Yang et al. (2018).

3.3 EKE trend

In consideration of the accelerated warming in the western boundary currents during the past 30 years (Wu et al. 2012; Hu et al. 2020), it is important to confirm whether the seasonality of EKE has changed in the KE region. Figure 9a shows the trend of surface annual mean EKE, in which the EKE level in the KE region depicts a positive (negative) trend on the northern (southern) flank of the jet. The area-mean EKE depicts no change in the upstream but increases in the downstream (based on 90% confidence level of the Student t-test; Fig. 9b and c). There is no clear difference in the trend for each season. Correlation coefficients between summer, winter, and annual mean EKE for the upstream and downstream are shown in Table 3. The six correlation coefficients are above 0.90 (statistically significant at the 90% level based on the Student t-test), indicating there are high correlations between the summer, winter, and annual-mean EKE. Thus, we will focus on the annual mean change in the following discussion. In addition to the area-mean EKE in the upstream and downstream regions, the trend of area-mean EKE in the entire KE (142° E–170° E, 31° N–39° N) is also estimated and an increasing trend is detected (statistically significant above the 90% confidence level; Fig. 9d).

To obtain a better understanding of the energy level, the change of surface total kinetic energy (TKE) is estimated (Fig. 10a). In accordance with EKE (Fig. 9a), the trend of TKE is also characterized with positive values north of the jet and negative values south of the jet, whereas the area-mean TKE has increased in the entire KE region (Fig. 10b). This consistency implies that the trend is not only a change in eddy activity but also a reflection of the change in the KE system: the KE has experienced a northward migration and intensification during the 21 years.

According to previous estimations, the evolution of KE system since the 1990s (Yang et al. 2016; Navarra and Lorenzo 2021) may be associated with the change of wind in the subtropical gyre (Cheon et al. 2012; Zhang et al. 2014) or decadal variability in the North Pacific (Qiu and Chen 2005; Qiu and Chen 2016) regulated by westward-propagating Rossby waves. The trends of zonal-mean wind stress curl from JRA-55 and ERA5 over the region (130° E–120° W, 15° N–65° N) are shown in Fig. 11a and b. Though the wind stress curl depicts

Table 2 The role of (a) advection and (b) pressure work at the boundaries (western, eastern, northern, and southern boundary) of the downstream KE (152° E–170° E, 31° N–39° N) in four seasons. The positive/negative value means energy is propagated into/out of the downstream via advection or pressure work. Note that units are different for advection and pressure work

(a) Advection (unit: 10^9 W)				
Domain	Spring	Summer	Autumn	Winter
Western boundary (152° E, 31° N–39° N)	4.85	5.96	4.88	4.33
Eastern boundary (170° E, 31° N–39° N)	−0.75	−0.42	−0.55	−0.53
Northern boundary (152° E–170° E, 39° N)	−0.75	−0.09	−0.03	0.01
Southern boundary (152° E–170° E, 31° N)	−0.21	−0.49	−0.11	−0.18
(b) Pressure work (unit: 10^{10} W)				
Domain	Spring	Summer	Autumn	Winter
Western boundary (152° E, 31° N–39° N)	1.90	2.14	2.39	1.66
Eastern boundary (170° E, 31° N–39° N)	−0.53	−0.64	−0.60	−0.38
Northern boundary (152° E–170° E, 39° N)	0.22	0.39	0.30	0.21
Southern boundary (152° E–170° E, 31° N)	−0.54	−0.74	−1.10	−0.65

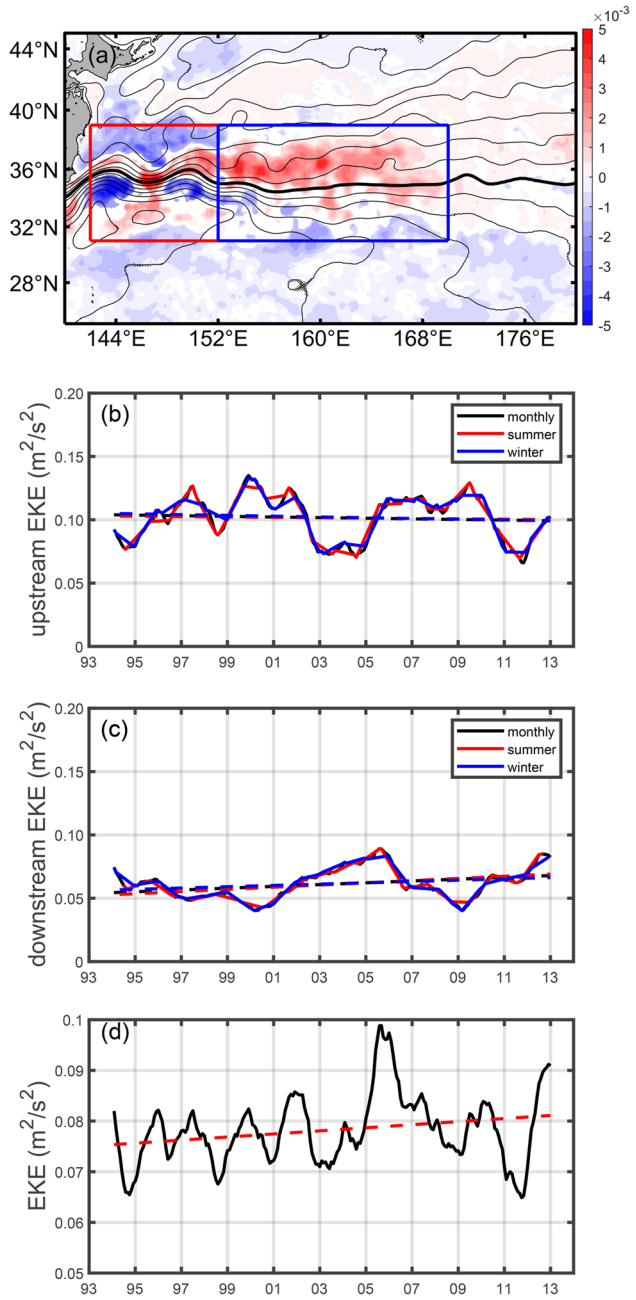

Fig. 9 **a** Spatial pattern of surface EKE trend (colored shading, $m^2 s^{-2}$ $year^{-1}$). The red box indicates the upstream KE region (142° E–152° E, 31° N–39° N) and blue box indicates the downstream KE region (152° E–170° E, 31° N–39° N). Regions where the trends cannot pass the 90% confidence level are marked as white color. Contours denote mean SSH field during 1993–2013. The black bold line denotes 0.4-m SSH contour, which indicates the KE jet. **b** The time series (curves) and linear trend (straight lines) of summer, winter, and monthly EKE in the upstream region. **c** Same as **b** but for the downstream region. **d** The time series and linear trend of monthly EKE in the entire KE region (142° E–170° E, 31° N–39° N). To remove mean seasonal cycle, the time series of monthly EKE is processed with 13-point smoothing. The first and last 12 monthly values of EKE are not used for the calculation of the trend. The trends of summer, winter, and monthly EKE in **c** are statistically insignificant above the 90% confidence level. The trends of summer, winter, and monthly EKE in **d** are statistically significant above the 90% confidence level based on the Student *t*-test

Table 3 Correlation coefficients between summer, winter, and annual mean EKE in the upstream and downstream KE region (statistically significant over the 90% level based on a Student *t*-test with 17 degrees of freedom)

Region	Variables	Correlation coefficient
Upstream	Summer and winter EKE	0.90
	Summer and annual EKE	0.99
	Winter and annual EKE	0.96
Downstream	Summer and winter EKE	0.91
	Summer and annual EKE	0.99
	Winter and annual EKE	0.97

a northward movement which favors the poleward shift of KE system, its weakening trend within the subtropical region (20° N–29° N latitude bands) is inconsistent with the intensification of the KE system. Therefore, the change of wind in the subtropical gyre cannot totally explain the change in the KE system. In comparison, we examine the Pacific Decadal Oscillation (PDO) index and the evolution of EKE in the 21 years following Qiu and Chen (2016). When the PDO index is positive, enhanced Ekman flux divergence generates negative local SSH anomalies to the east of the KE region in 170° W–160° W along the zonal band of 32° N–34° N (Fig. 12a and b). As negative SSH anomaly signals propagate westward in terms of Rossby waves into the KE region after a delay of 3–4 years, the KE jet inflow is forced southward and rides over the ridge through a shallow segment (Qiu and Chen 2005), leading to an unstable state of the KE system with an active (low-energy) EKE field in the upstream (downstream). During the negative PDO index phase, on the other hand, positive SSH anomalies are generated through the Ekman flux convergence. After propagating into the KE region, these positive anomalies force the inflow northward, leading to a stable state of the KE system with a low-energy (active) eddy field in the upstream (downstream). From Fig. 12c and d, we learn that surface EKE in the upstream (downstream) depicts a crest during 1999–2002/2005–2010 (2002–2006/2010–2013) and a trough in 2002–2005/2010–2012 (1996–2001/2006–2010), matching the evolution of SSH in Fig. 12b associated with PDO. Therefore, the EKE evolution during 1993–2013 reflects the decadal variability of the KE system.

4 Summary

Based on an eddy-resolving reanalysis product, this study investigates the mechanisms underlying the seasonal modulation of mesoscale eddy activity in the Kuroshio

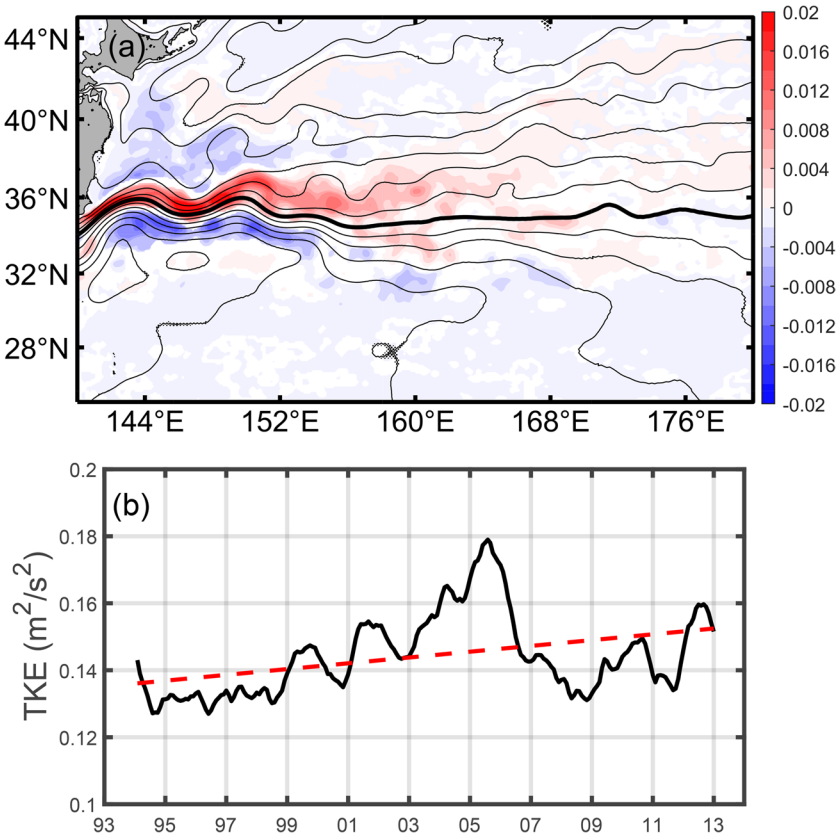

Fig. 10 **a** Spatial pattern of surface monthly total kinetic energy (TKE) trend (colored shading, m^2s^{-2} $year^{-1}$). Regions where the trends cannot pass the 90% confidence level are marked as white color. Contours are as noted in Fig. 9a. **b** The time series and linear trend of monthly TKE in the entire KE region (142° E–170° E, 31° N–39° N). To remove mean seasonal cycle, the time series of monthly TKE is processed with 13-point smoothing. The first and last 12 monthly values of TKE are not used for the calculation of the trend. The trend is statistically significant above the 90% confidence level based on the Student *t*-test

Extension region and explores the change in eddy kinetic energy during 1993–2013. The major results of this study are summarized as follows:

1. In four seasons, a high energy level is found to appear at larger meridional (zonal) wavenumber range in the upstream (downstream) Kuroshio Extension, indicating that eddies are more zonally (meridionally) elongated.
2. In the upstream region, baroclinic instability associated with horizontal buoyancy flux plays a predominant role in regulating the seasonal evolution of eddy kinetic energy. In the downstream region, non-local energy exchange associated with pressure work is the main source of eddy kinetic energy.
3. During 1993–2013, the seasonality of eddy kinetic energy in the Kuroshio Extension remains unchanged.

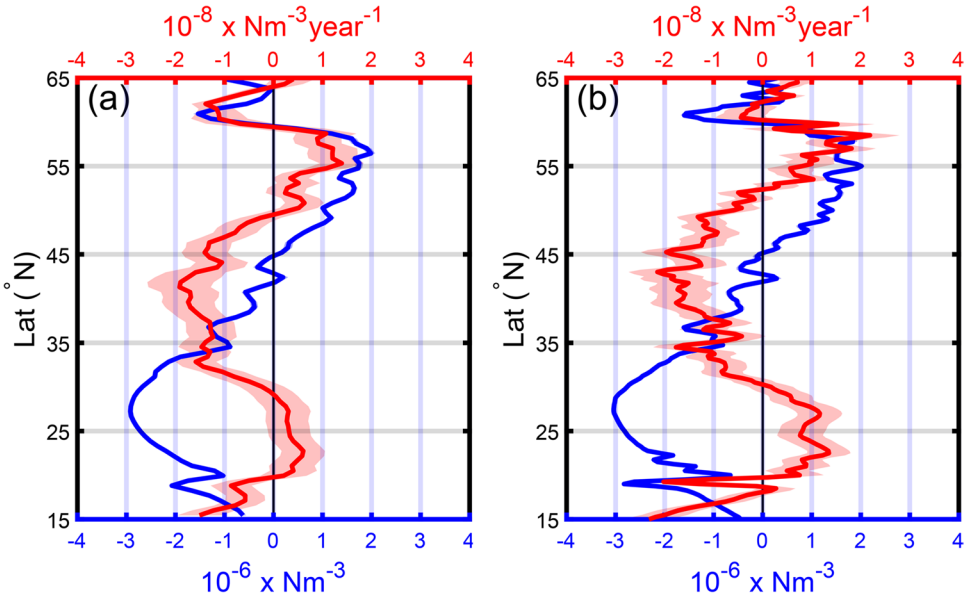

Fig. 11 Mean value (blue solid line) and trend (red solid line) of zonal-average wind stress curl over the region (130° E–120° W, 15° N–65° N) derived from **a** JRA-55 and **b** ERA5 during 1993–2013. Following Trenberth et al. (1990), wind stress curl is calculated on the basis of zonal and meridional wind velocity. To remove mean seasonal cycle, the time series of wind stress curl is processed with 13-point smoothing. Shading indicates standard error (blue shading) and the 90% confidence interval of the trend (red shading)

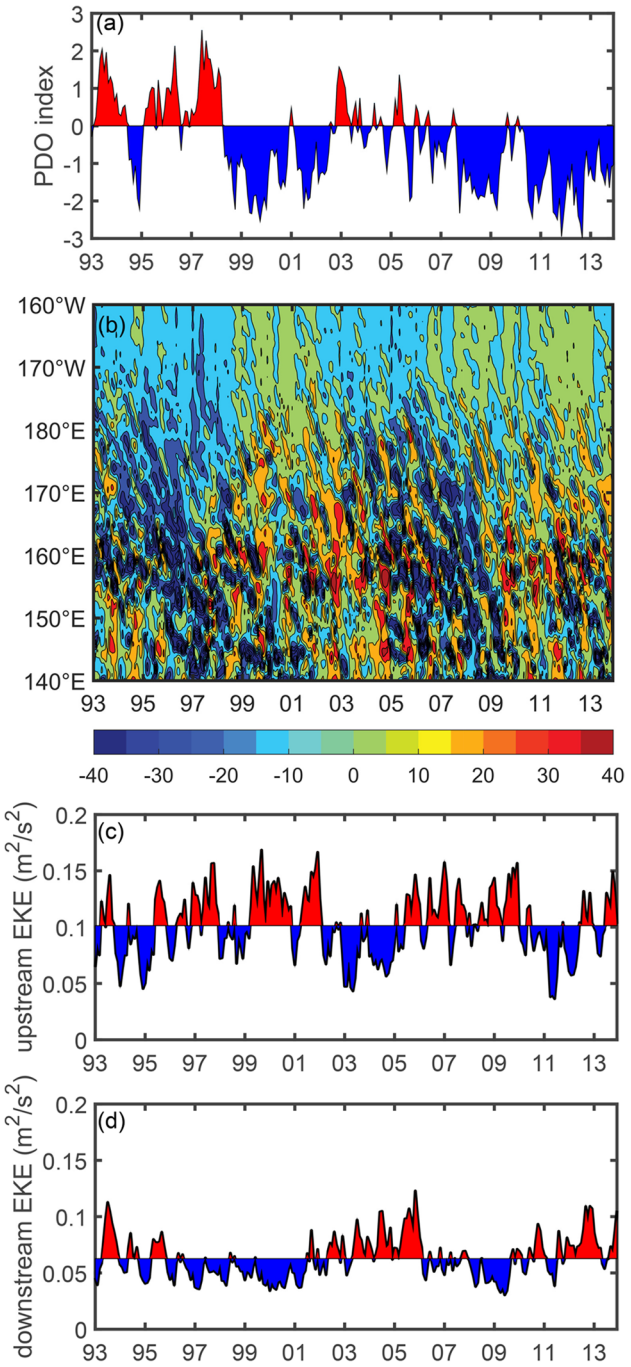

Fig. 12 **a** Time series of the Pacific Decadal Oscillation (PDO) index from https://www.ncei.noaa.gov/pub/data/cmb/ersst/v5/index/ersst.v5.pdo.dat. **b** Time-longitude pattern of monthly SSH anomalies (cm) along the zonal band of 32° N–34° N from FORA. The time series of monthly EKE in the **c** upstream and **d** downstream KE region

There is no change of eddy kinetic energy in the upstream region, while eddy kinetic energy in the downstream region increases significantly. The evolution is a reflection of the decadal variability of the Kuroshio Extension system associated with the Pacific Decadal Oscillation.

This study has explored the seasonal variability of eddy activity in the Kuroshio Extension, which is likely beneficial to the understanding of ocean dynamics in this region. In addition, it should also be noted that longer data is required to confirm the response of the seasonality of eddy kinetic energy to global warming. Moreover, the process of eddy energy dissipation is not analyzed here, which should be investigated in detail in the future. Besides, the meandering of flow is treated as mesoscale eddy when eddy kinetic energy is calculated based on velocity anomaly. The effect of the meandering will be considered in the future. Furthermore, previous studies have shown that air-sea interaction in the Kuroshio Extension may affect eddy activity (Ma et al. 2016; Yang et al. 2019; Shan et al. 2020). The seasonal variability of eddy-atmosphere interactions and their potential role in oceanic energy balance should be studied based on high-resolution coupled models in the future.

Acknowledgements This work has been carried out at Physical Oceanography Laboratory/Ocean University of China, China. The authors would like to thank the laboratory for providing all the needed support to carry out this research. All the analysis and plotting are done in MATLAB.

Funding This research is supported by the National Natural Science Foundation of China (42176006, 42076009, and 41922039) and Fundamental Research Funds for the Central Universities (202241006 and 202072001).

Data availability The datasets generated and/or analyzed in the current study are available from the corresponding author on reasonable request. The following datasets are used for the analysis: FORA-WNP30 dataset is downloaded from http://synthesis.jamstec.go.jp/FORA/e/, and JRA-55 is downloaded from https://rda.ucar.edu/datasets/ds628.1/. Satellite data is sourced from https://www.aviso.altimetry.fr/ and ECMWF ERA5 is sourced from https://cds.climate.copernicus.eu/cdsapp#!/dataset/reanalysis-era5-single-levels-monthly-means?tab=overview. The climate index of PDO is sourced from https://www.ncei.noaa.gov/pub/data/cmb/ersst/v5/index/ersst.v5.pdo.dat.

Code availability Codes for the energy budget can be available from the corresponding author.

Declarations

Conflict of interest The authors declare no conflict of interest.

References

Belmonte Rivas M, Stoffelen A (2019) Characterizing ERA-Interim and ERA5 surface wind biases using ASCAT. Ocean Sci 15:831–852. https://doi.org/10.5194/os-15-831-2019

Berloff P, McWilliams J (1999) Large-scale, low-frequency variability in wind-driven ocean gyres. J Phys Oceanogr 29:1925–1949

Bishop SP (2013) Divergent eddy heat fluxes in the Kuroshio Extension at 144° -148° E. Part II: spatiotemporal variability. J Phys Oceanogr 43(11):2416–2431

Ceballos LI, Di Lorenzo E, Hoyos CD et al (2009) North Pacific Gyre Oscillation synchronizes climate fluctuations in the eastern and western boundary systems. J Climate 22:5163–5174. https://doi.org/10.1175/2009JCLI2848.1

Chen R, Flierl GR, Wunsch C (2014) A description of local and nonlocal eddy-mean flow interaction in a global eddy-permitting

state estimate. J Phys Oceanogr 44:2336–2352. https://doi.org/10.1175/JPO-D-14-0009.1
Cheon WG, Park Y-G, Yeh S-W, Kim B-M (2012) Atmospheric impact on the northwestern Pacific under a global warming scenario: the Kuroshio-Oyashio Extension. Geophys Res Lett 39:n/a-n/a. https://doi.org/10.1029/2012GL052364
Cornillon P, Park K-A (2001) Warm core ring velocities inferred from NSCAT. Geophys Res Lett 28:575–578. https://doi.org/10.1029/2000GL011487
Cronin MF, Bond NA, Thomas Farrar J et al (2013) Formation and erosion of the seasonal thermocline in the Kuroshio Extension Recirculation Gyre. Deep Sea Res Part II 85:62–74. https://doi.org/10.1016/j.dsr2.2012.07.018
Deser C, Alexander MA, Timlin MS (1999) Evidence for a wind-driven intensification of the Kuroshio Current extension from the 1970s to the 1980s. J Climate 12:1697–1706
Dong D, Brandt P, Chang P et al (2017) Mesoscale eddies in the Northwestern Pacific Ocean: three-dimensional eddy structures and heat/salt transports. J Geophys Res Oceans 122:9795–9813. https://doi.org/10.1002/2017JC013303
Ducet N, Le Traon P-Y (2001) A comparison of surface eddy kinetic energy and Reynolds stresses in the Gulf Stream and the Kuroshio Current systems from merged TOPEX/Poseidon and ERS-1/2 altimetric data. J Geophys Res 106:16603–16622. https://doi.org/10.1029/2000JC000205
Gill AE, Green JSA, Simmons AJ (1974) Energy partition in the large-scale ocean circulation and the production of mid-ocean eddies. Deep-Sea Res Oceanogr Abstr 21:499–528
Harada Y, Kamahori H, Kobayashi C et al (2016) The JRA-55 Reanalysis: representation of atmospheric circulation and climate variability. J Meteorol Soc JPN 94:269–302. https://doi.org/10.2151/jmsj.2016-015
Hersbach H, Bell B, Berrisford P et al (2020) The ERA5 global reanalysis. QJR Meteorol Soc 146:1999–2049. https://doi.org/10.1002/qj.3803
Hu S, Sprintall J, Guan C, et al (2020) Deep-reaching acceleration of global mean ocean circulation over the past two decades. Sci Adv 6:eaax7727. https://doi.org/10.1126/sciadv.aax7727
Huang P (2015) Seasonal changes in tropical SST and the surface energy budget under global warming projected by CMIP5 models. J Climate 28:6503–6515. https://doi.org/10.1175/JCLI-D-15-0055.1
Itoh S, Yasuda I (2010) Characteristics of mesoscale eddies in the Kuroshio-Oyashio Extension Region detected from the distribution of the sea surface height anomaly. J Phys Oceanogr 40:1018–1034
Imawaki S, Uchida H, Ichikawa H et al (2001) Satellite altimeter monitoring the Kuroshio Transport south of Japan. Geophys Res Lett 28:17–20. https://doi.org/10.1029/2000GL011796
Jayne SR, Hogg NG, Waterman SN et al (2009) The Kuroshio Extension and its recirculation gyres. Deep Sea Res Part I 56:2088–2099
Ji J, Dong C, Zhang B et al (2018) Oceanic eddy characteristics and generation mechanisms in the Kuroshio Extension region. J Geophys Res Oceans 123:8548–8567. https://doi.org/10.1029/2018JC014196
Jiang W, Peng L, Jin T, Zhang S (2017) Variability of the Kuroshio Extension system in 1992–2013 from satellite altimetry data. Geodesy Geodynam 8:103–110. https://doi.org/10.1016/j.geog.2016.12.004
Jing Z, Chang P, Shan X et al (2019) Mesoscale SST dynamics in the Kuroshio-Oyashio Extension region. J Phys Oceanogr 49:1339–1352
Kalverla PC, Duncan JB Jr, Steeneveld G-J, Holtslag AAM (2019) Low-level jets over the North Sea based on ERA5 and observations: together they do better. Wind Energ Sci 4:193–209. https://doi.org/10.5194/wes-4-193-2019
Kelly KA, Small RJ, Samelson RM et al (2010) Western boundary currents and frontal air-sea interaction: Gulf Stream and Kuroshio Extension. J Climate 23:5644–5667. https://doi.org/10.1175/2010JCLI3346.1
Kobayashi S, Ota Y, Harada Y et al (2015) The JRA-55 reanalysis: general specifications and basic characteristics. J Meteorol Soc Japan 93:5–48
Kwon Y-O, Deser C (2007) North Pacific decadal variability in the Community Climate System Model version 2. J Climate 20:2416–2433
Lan J, Xu L, Guo P (2003) Seasonal variability in the Kuroshio Extension current system. J Ocean Univ China 2:129–133. https://doi.org/10.1007/s11802-003-0040-1
Long Y, Zhu X, Guo X et al (2021) Variations of the Kuroshio in the Luzon Strait revealed by EOF analysis of repeated XBT data and sea-level anomalies. J Geophys Res Oceans 126:e2020JC016849
Ma X, Jing Z, Chang P et al (2016) Western boundary currents regulated by interaction between ocean eddies and the atmosphere. Nature 535:533–537
Marshall DP, Maddison JR, Berloff PS (2012) A framework for parameterizing eddy potential vorticity fluxes. J Phys Oceanogr 42:539–557
Matsuta T, Masumoto Y (2021) Modified view of energy budget diagram and its application to the Kuroshio Extension region. J Phys Oceanogr 51:1163–1175. https://doi.org/10.1175/JPO-D-20-0124.1
Meng Y, Liu H, Lin P et al (2021) Oceanic mesoscale eddy in the Kuroshio Extension: comparison of four datasets. Atmos Sci Lett 14:100011
Miao H, Dong D, Huang G, et al (2020) Evaluation of Northern Hemisphere surface wind speed and wind power density in multiple reanalysis datasets. Energy 200:117382. https://doi.org/10.1016/j.energy.2020.117382
Miller AJ, Cayan DR, White WB (1998) A westward-intensified decadal change in the North Pacific thermocline and gyre-scale circulation. J Climate 11:3112–3127
Nakamura H, Isobe A, Minobe S et al (2015) "Hot Spots" in the climate system-new developments in the extratropical ocean-atmosphere interaction research: a short review and an introduction. J Oceanogr 71:463–467
Navarra GG, Di Lorenzo E (2021) Poleward shift and intensified variability of Kuroshio-Oyashio extension and North Pacific Transition Zone under climate change. Clim Dyn 56:2469–2486. https://doi.org/10.1007/s00382-021-05677-0
Noh Y, Jin Kim H (1999) Simulations of temperature and turbulence structure of the oceanic boundary layer with the improved near-surface process. J Geophys Res 104:15621–15634. https://doi.org/10.1029/1999JC900068
Noh Y, Yim BY, You SH et al (2007) Seasonal variation of eddy kinetic energy of the North Pacific Subtropical Countercurrent simulated by an eddy-resolving OGCM. Geophys Res Lett 34:L07601. https://doi.org/10.1029/2006GL029130
Nonaka M, Xie S-P (2003) Covariations of sea surface temperature and wind over the Kuroshio and its extension: evidence for ocean-to-atmosphere feedback. J Climate 16:1404–1413
Olauson J (2018) ERA5: the new champion of wind power modelling? Renewable Energy 126:322–331. https://doi.org/10.1016/j.renene.2018.03.056
Qiu B (2003) Kuroshio Extension variability and forcing of the Pacific Decadal Oscillations: responses and potential feedback. J Phys Oceanogr 33:2465–2482
Qiu B, Chen S (2005) Variability of the Kuroshio Extension jet, recirculation gyre, and mesoscale eddies on decadal time scales. J Phys Oceanogr 35:2090–2103. https://doi.org/10.1175/JPO2807.1

Qiu B, Chen S (2016) Inter-decadal modulations in the dynamical state of the Kuroshio Extension system: 1905–2015. CLIVAR Exchanges 20:7–9
Qiu B, Kelly KA (1993) Upper-Ocean heat balance in the Kuroshio Extension region. J Phys Oceanogr 23:2027–2041
Qiu B, Scott RB, Chen S (2008) Length scales of eddy generation and nonlinear evolution of the seasonally modulated South Pacific Subtropical Countercurrent. J Phys Oceanogr 38:1515–1528. https://doi.org/10.1175/2007JPO3856.1
Qiu B, Chen S, Schneider N, Taguchi B (2014) A coupled decadal prediction of the dynamic state of the Kuroshio Extension system. J Climate 27:1751–1764. https://doi.org/10.1175/JCLI-D-13-00318.1
Sasaki YN, Minobe S (2015) Climatological mean features and interannual to decadal variability of ring formations in the Kuroshio Extension region. J Oceanogr 71:499–509
Sasaki YN, Schneider N (2011) Decadal shifts of the Kuroshio Extension jet: application of thin-jet theory. J Phys Oceanogr 41:979–993. https://doi.org/10.1175/2011JPO4550.1
Sasaki YN, Minobe S, Schneider N (2013) Decadal response of the Kuroshio Extension jet to Rossby waves: observation and thin-jet theory. J Phys Oceanogr 43:442–456. https://doi.org/10.1175/JPO-D-12-096.1
Scharffenberg MG, Stammer D (2010) Seasonal variations of the large-scale geostrophic flow field and eddy kinetic energy inferred from the TOPEX/Poseidon and Jason-1 tandem mission data. J Geophys Res 115:C02008
Seager R, Kushnir Y, Naik NH et al (2001) Wind-driven shifts in the latitude of the Kuroshio-Oyashio Extension and generation of SST anomalies on decadal timescales. J Climate 14:4249–4265
Shan X, Jing Z, Sun B, Wu L (2020) Impacts of ocean current-atmosphere interactions on mesoscale eddy energetics in the Kuroshio Extension region. Geosci Lett 7:3. https://doi.org/10.1186/s40562-020-00152-w
Stammer D (1998) On eddy characteristics, eddy transports, and mean flow properties. J Phys Oceanogr 28:727–739
Stammer D, Wunsch C (1999) Temporal changes in eddy energy of the oceans. Deep Sea Res Part II 46:77–108. https://doi.org/10.1016/S0967-0645(98)00106-4
Tai CK, White WB (1990) Eddy variability in the Kuroshio Extension as revealed by Geosat altimetry: energy propagation away from the jet, Reynolds stress, and seasonal cycle. J Phys Oceanogr 20(20):1761–1777
Trenberth KE, Large WG, Olson JG (1990) The mean annual cycle in global ocean wind stress. J Phys Oceanogr 20:1742–1760
Tsujino H, Usui N, Nakano H (2006) Dynamics of Kuroshio path variations in a high-resolution general circulation model. J Geophys Res 111:C11001. https://doi.org/10.1029/2005JC003118
Usui N, Wakamatsu T, Tanaka Y et al (2017) Four-dimensional variational ocean reanalysis: a 30-year high-resolution dataset in the western North Pacific (FORA-WNP30). J Oceanogr 73(2):205–233
Vivier F, Kelly KA, Thompson LA (2002) Heat budget in the Kuroshio Extension region: 1993–99. J Phys Oceanogr 32:3436–3454. https://doi.org/10.1175/1520-0485(2002)032%3c3436:HBITKE%3e2.0.CO;2
Von Storch J-S, Eden C, Fast I et al (2012) An estimate of the Lorenz energy cycle for the world ocean based on the STORM/NCEP simulation. J Phys Oceanogr 42:2185–2205. https://doi.org/10.1175/JPO-D-12-079.1
Wang M, Du Y, Qiu B et al (2017) Mechanism of seasonal eddy kinetic energy variability in the eastern equatorial Pacific Ocean. J Geophys Res Oceans 122:3240–3252. https://doi.org/10.1002/2017JC012711
Wang Q, Pierini S (2020) On the role of the Kuroshio Extension bimodality in modulating the surface eddy kinetic energy seasonal variability. Geophys Res Lett 47:e2019GL086308. https://doi.org/10.1029/2019GL086308
Wang Q, Tang Y (2022) The interannual variability of eddy kinetic energy in the Kuroshio large meander region and its relationship to the Kuroshio latitudinal position at 140°E. J Geophys Res Oceans 127:e2021JC017915
Wang J, Guan Y, Wu L et al (2021) Changing lengths of the four seasons by global warming. Geophys Res Lett 48:e2020GL091753
Waterman S, Hoskins BJ (2013) Eddy shape, orientation, propagation, and mean flow feedback in western boundary current jets. J Phys Oceanogr 43:1666–1690. https://doi.org/10.1175/JPO-D-12-0152.1
Waterman S, Hogg NG, Jayne SR (2011) Eddy-mean flow interaction in the Kuroshio Extension region. J Phys Oceanogr 41:1182–1208. https://doi.org/10.1175/2010JPO4564.1
Wijffels SE, Hall MM, Joyce T et al (1998) Multiple deep gyres of the western North Pacific: a WOCE section along 149°E. J Geophys Res 103:12985–13009. https://doi.org/10.1029/98JC01016
Wu L, Cai W, Zhang L et al (2012) Enhanced warming over the global subtropical western boundary currents. Nat Clim Chang 2:161–166
Xu H, Tokinaga H, Xie S-P (2010) Atmospheric Effects of the Kuroshio Large Meander during 2004–05. J Climate 23:4704–4715
Yang Y, San Liang X (2018) On the seasonal eddy variability in the Kuroshio Extension. J Phys Oceanogr 48:1675–1689. https://doi.org/10.1175/JPO-D-18-0058.1
Yang H, Wu L (2012) Trends of upper-layer circulation in the South China Sea during 1959–2008. J Geophys Res 117:C08037. https://doi.org/10.1029/2012JC008068
Yang H, Lohmann G, Wei W et al (2016) Intensification and poleward shift of subtropical western boundary currents in a warming climate. J Geophys Res Oceans 121:4928–4945. https://doi.org/10.1002/2015JC011513
Yang Y, San Liang X, Qiu B, Chen S (2017) On the decadal variability of the eddy kinetic energy in the Kuroshio Extension. J Phys Oceanogr 47:1169–1187. https://doi.org/10.1175/JPO-D-16-0201.1
Yang H, Qiu B, Chang P et al (2018) Decadal variability of eddy characteristics and energetics in the Kuroshio Extension: unstable versus stable states. J Geophys Res Oceans 123:6653–6669. https://doi.org/10.1029/2018JC014081
Yang H, Chang P, Qiu B et al (2019) Mesoscale air-sea interaction and its role in eddy energy dissipation in the Kuroshio Extension. J Climate 32:8659–8676. https://doi.org/10.1175/JCLI-D-19-0155.1
Zhai X (2017) The annual cycle of surface eddy kinetic energy and its influence on eddy momentum fluxes as inferred from altimeter data. Satell Oceanogr Meteorol 2:299. https://doi.org/10.18063/som.v2i2.299
Zhang X, Church JA, Platten SM, Monselesan D (2014) Projection of subtropical gyre circulation and associated sea level changes in the Pacific based on CMIP3 climate models. Clim Dyn 43:131–144. https://doi.org/10.1007/s00382-013-1902-x